

In the format provided by the authors and unedited.

# Electronic correlations in twisted bilayer graphene near the magic angle

Youngjoon Choi<sup>1,2,3</sup>, Jeannette Kemmer<sup>1,2</sup>, Yang Peng<sup>2,3,4</sup>, Alex Thomson<sup>2,3,4</sup>, Harpreet Arora<sup>1,2</sup>, Robert Polski<sup>1,2</sup>, Yiran Zhang <sup>1,2,3</sup>, Hechen Ren<sup>1,2</sup>, Jason Alicea<sup>2,3,4</sup>, Gil Refael<sup>2,3,4</sup>, Felix von Oppen<sup>2,5</sup>, Kenji Watanabe <sup>6</sup>, Takashi Taniguchi<sup>6</sup> and Stevan Nadj-Perge <sup>1,2\*</sup>

---

<sup>1</sup>T. J. Watson Laboratory of Applied Physics, California Institute of Technology, Pasadena, CA, USA. <sup>2</sup>Institute for Quantum Information and Matter, California Institute of Technology, Pasadena, CA, USA. <sup>3</sup>Department of Physics, California Institute of Technology, Pasadena, CA, USA. <sup>4</sup>Walter Burke Institute for Theoretical Physics, California Institute of Technology, Pasadena, CA, USA. <sup>5</sup>Dahlem Center for Complex Quantum Systems and Fachbereich Physik, Freie Universität Berlin, Berlin, Germany. <sup>6</sup>National Institute for Materials Science, Tsukuba, Ibaraki, Japan. \*e-mail: [s.nadj-perge@caltech.edu](mailto:s.nadj-perge@caltech.edu)

**Supplementary information for “Electronic Correlations in Twisted Bilayer Graphene Near the Magic Angle”**

**Authors:** Youngjoon Choi, Jeannette Kemmer, Yang Peng, Alex Thomson, Harpreet Arora, Robert Polski, Yiran Zhang, Hechen Ren, Jason Alicea, Gil Refael, Felix von Oppen, Kenji Watanabe, Takashi Taniguchi and Stevan Nadj-Perge

Table of contents

Section 1: Sample fabrication and measurement details .....	1
Section 2: Data on 4.8nm moiré pattern .....	1
Section 3: Tip-related effects .....	2
Section 4: Tip-gating correction at the CNP and the enhancement of the width .....	7
Section 5: Areas with different twist angle $\theta$ .....	9
Section 6: Additional data .....	10
Section 7: Theoretical modeling .....	12
References: .....	29

## Supplementary Text

### Section 1: Sample fabrication and measurement details

Figure S1 outlines the fabrication steps for twisted bilayer graphene (TBG). We used the tear-and-twist technique following similar procedures outlined in Refs 1-3. After picking up a 30-50nm-thick boron nitride flake using Polydimethylsiloxane (PDMS) coated with a Poly(bisphenol A carbonate) (PC) polymer, the graphene is torn into two parts which were subsequently picked up while controlling the twist between the parts. The entire stack is then transferred onto a separate PDMS film in order to flip the order of the layers (Fig. S1 left panel). In this step, PC is dissolved in N-Methyl-2-pyrrolidone (NMP). Afterward the PDMS with the inverted stack structure is transferred onto a prepared chip (silicon chip covered with 300nm of silicon-oxide) with pre-patterned electrodes and a 10nm thick metallic graphene multilayer that is used as the back gate (Fig. S1 right panel). The twisted bilayer graphene (TBG) is then contacted to the gold electrodes using additional few-layer graphene contacts. During device fabrication special care is taken so that the temperature of the sample never exceeds 150°C to avoid untwisting of the TBG <sup>4</sup>.

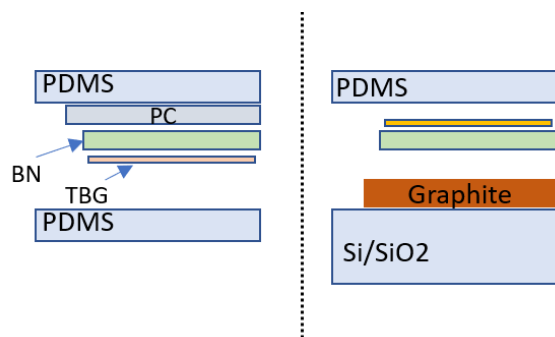


Figure S1. Critical steps of the device fabrication sequence. After picking up the BN and graphene flakes, the stack is transferred and flipped onto a second PDMS stamp that is used for a second transfer onto the graphite back gate. In a separate step, few-layer graphene is transferred to contact TBG with a bias electrode.

### Section 2: Data on 4.8nm moiré pattern

Figure S2 shows a  $dI/dV$  map for the  $L_M = 4.8\text{nm}$  (device D2) moiré pattern. The charge neutrality point and both  $vHs$  peaks move in parallel following the quadratic relation between charge density  $n$  and chemical potential  $\mu$ ,  $|n| = \alpha \mu^2$  (up to an offset in  $V_{\text{Bias}}$  and  $V_{\text{Bg}}$ ). This suggests that in this regime the density of states between the  $vHs$  peaks follows approximately a linear dispersion as expected for large twist angles. The vertical offset between the two branches is a

consequence of tip-induced gating, which is explained in the following section. We note that this effect may explain the apparent small increase in the distance between the van Hove singularities at the CNP observed in Ref. 5. Importantly, the relative enhancement of the peak splitting for angles close to the magic angle value is too large to be explained by this effect as discussed in Section 4.

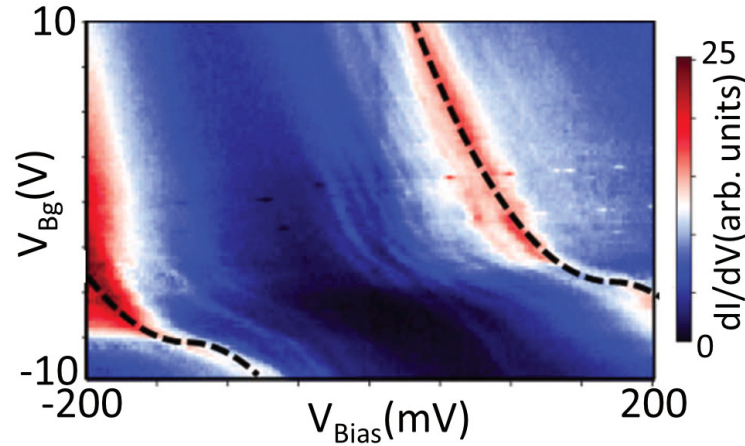


Figure S2. Spectroscopy data taken on the AA site for  $\theta \approx 3^\circ$ , device D2. Dashed lines correspond to a fit  $|n| = \alpha\mu^2$  where  $\mu = -eV_{\text{Bias}}$  and  $n = C_{\text{Bg}} V_{\text{Bg}}$ . The small vertical offset of the two branches that give rise to a small enhancement in splitting in the  $V_{\text{Bias}}$  direction that is due to tip gating as discussed in the following section.

### Section 3: Tip-related effects

#### Dynamic strain effects

Occasionally we observe topographies with pronounced hysteresis, especially for parameters when the STM tip-sample distance is reduced (for example  $V_{\text{Bias}} = \pm 200 \text{ mV}$ , set point current 100pA or more). Similar STM-tip-induced strain effects have been previously reported for moiré patterns in single-layer graphene/boron nitride heterostructures<sup>6</sup> as well as in graphene on silicon oxide<sup>7</sup>. The intuitive understanding of this effect is that when the interaction between the tip and the sample is strong, the tip can slightly displace the carbon atoms as it scans over the surface and consequently shift the moiré pattern boundaries. We have performed a similar analysis as in Ref. 6 and obtained strain maps illustrating this effect (see Fig. S3). In addition to

these strain-related effects, we have also observed other signatures of tip-graphene interaction, such as hysteresis in the current vs height relation  $I(z)$ .

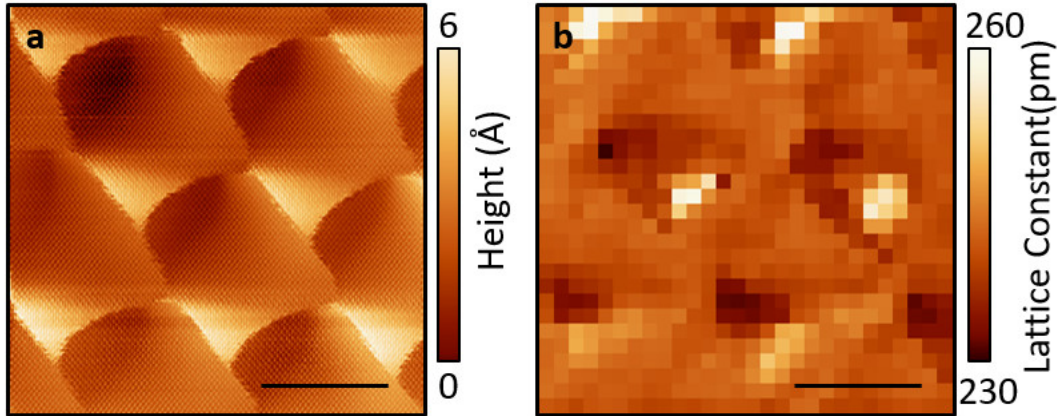


Figure S3. (a) The topography of the strained region close to the magic angle ( $L_M = 13\text{nm}$ ) in device D1 and the corresponding strain map (b). The map represents the local lattice constant obtained by coarsening the topography grid into discrete pixels and performing a Fourier analysis of the  $3\text{nm} \times 3\text{nm}$  area around each pixel and selecting one particular direction. Other directions show a similar dependence. Scale bar is  $10\text{nm}$  for both plots.

The dynamic strain effects are not observed consistently throughout both samples. The strain is typically observed in areas close to the magic angle in device D1 and in certain areas away from the magic angle in device D2. Also, in regions close to the magic angle in device D2, the moiré superlattice is more uniform and there is overall less strain. From these observations we conclude that the presence of intrinsic external strain is needed in order to observe the dynamic tip-induced strain effect. Different STM microtips may have different sensitivities to these effects. Importantly, we do not see a qualitative difference in the spectroscopy data between the two devices indicating that these effects do not play a significant role in determining the local density of states. This is consistent with the previously reported observations in Ref.6. While this effect produces artifacts in the topography, it does not change it permanently so the distance between AA sites and hence the twist angle  $\theta$  can still be obtained accurately.

## Effects of tip screening

Due to the close proximity between the STM tip and the sample, one might expect that the presence of metallic objects will facilitate screening of electronic correlations. In this section, we estimate the strength of the electron-electron interaction in this system. Indeed, in the presence of the metal tip which provides additional screening the interaction energy scale can be greatly suppressed compared to the pristine unscreened case. A naïve estimate for the electrostatic energy for two electrons placed  $L_M = 13\text{nm}$  apart is given by  $e^2/(4\pi\epsilon\epsilon_{\text{BN}}L_M) = 36\text{meV}$ . This estimate is enhanced further to approximately  $50\text{meV}$  if we consider that we have the boron nitride dielectric only on one side. However, in the presence of a metallic tip this interaction is locally screened considerably. For a tip-sample distance of  $1\text{nm}$  (taken as an upper limit), the Coulomb-energy scale would scale as  $(1/L_M - 1/\sqrt{L_M^2 + 4z_{\text{tip}}^2})$  resulting in an interaction energy of  $0.5\text{meV}$  for  $L_M = 13\text{nm}$ . More precise estimates for the decay of the Coulomb interaction are presented in Figure S4 as obtained by electrostatic simulations that take into account the presence of the metallic tip and the surrounding dielectric. The values of  $\sim 10\text{mV}$  extracted from comparing our experimental results to the model calculations presented in the main text are consistent with these estimates.

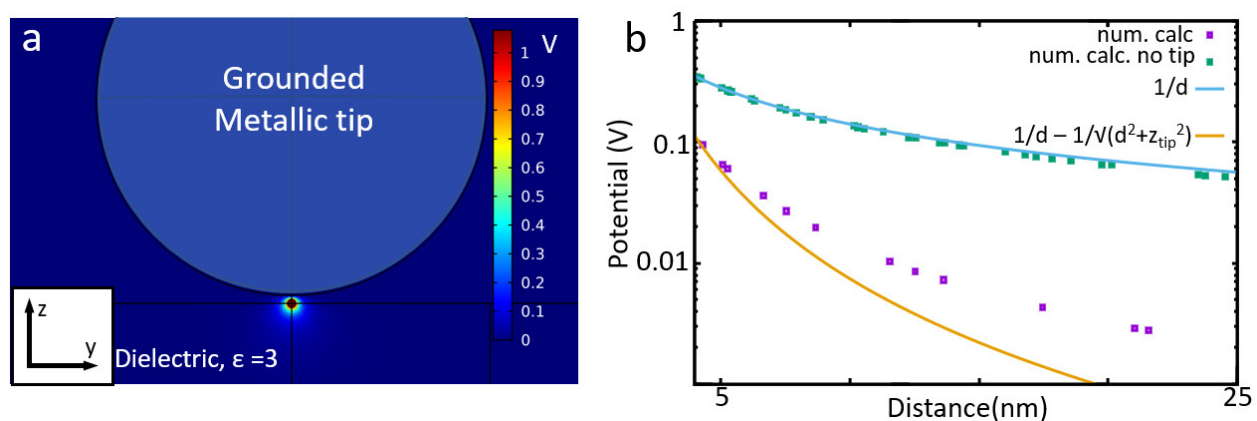


Figure S4. (a) 3D Electrostatic simulation of the potential that takes into account the tip-sample geometry. Blue circle represents a metallic tip with fixed potential  $V = 0$  and the rectangle corresponds to the dielectric slab. The small circle was charged by  $1.6\text{e-}19\text{C}$  and the slice represents the decay of the potential along the  $y$ - $z$  direction. (b) Decay of the potential as a function of distance. Different lines correspond to numerical calculations with and without the tip as well as theoretical estimates corresponding to  $1/d$  decay and  $(1/d - 1/(d^2 + 4z_{\text{tip}}^2)^{1/2})$  decay.

### Tip-induced gating and work function difference between TBG and the tip

It is established that the STM tip can change the local potential in semiconducting samples due to a finite screening length as observed in InAs<sup>8</sup>, monolayer and bilayer graphene in magnetic field<sup>9</sup>, as well as other semiconducting systems. We have systematically observed the formation of quantum dots in the regions close to the magic angle indicative of the formation of insulating states. The induced quantum dots introduce a series of sharp resonances observed as almost horizontal lines crossing the features in  $V_{\text{Bias}}$  vs  $V_{\text{Bg}}$  conductance maps.

The observed resonance can be utilized to characterize the electrostatic properties of the quantum dot and determine the capacitance of the tip  $C_{\text{Tip}}$  and the work-function difference between the tip and the twisted bilayer graphene. To this end, we take measurements at different tip heights, i.e., different set points. Figure S5 shows a typical spectrum on an AA site for two different set currents of 100pA and 1nA. Lines (indicated by arrows) mark some of the resonances originating from the quantum dots. The slope of the lines directly measures the ratio between the tip and the back-gate capacitances  $C_{\text{Tip}}/C_{\text{Bg}}$ , and it is approximately 20 for device D2. The tip capacitance changes when the tip moves closer to the sample. This is reflected in a change of the  $V_{\text{Bias}}/V_{\text{Bg}}$  slope. Another effect observed is the overall shift of the positions in point spectroscopy  $V_{\text{Bias}}$  vs.  $V_{\text{Bg}}$  plots for which the upper flat band touches the Fermi level and also the position of charge neutrality. The shift of these points indicates that tip-induced gating changes the electron density underneath the tip in a manner that depends on the tip-sample distance. This effect is a consequence of a difference between the work functions of the metallic tip and the twisted bilayer graphene.

In a simple model, the charge density of the TBG underneath the tip can be written as:

$$n(r, z) = C_{\text{Bg}}(V_{\text{Bg}} - V_{\text{Bias}}) - C_{\text{Tip}}(r, z)(V_{\text{Bias}} - \Delta\Phi),$$

where  $\Delta\Phi$  is the work-function difference between the tip and the sample. Specifically, when the tip moves closer, the charge neutrality point moves towards more negative voltages ( $V_{\text{Bg}}=-6.8$  V at CNP for 100pA setpoint and  $V_{\text{Bg}}=-8.6$  V at CNP for 1nA). Also, the slope of the lines changes, reflecting a change in the capacitance ( $C_{\text{Tip}}/C_{\text{Bg}} = 20$  for 100pA setpoint and 24 for 1nA setpoint).

By solving the equation for the charge density at charge neutrality for two setpoints, one gets an estimate for  $\Delta\Phi = 150\text{-}200\text{mV}$ . We note that the STM tips in our measurements are prepared on a silver crystal that has a smaller work function compared to graphene which results in the observed n-type doping.

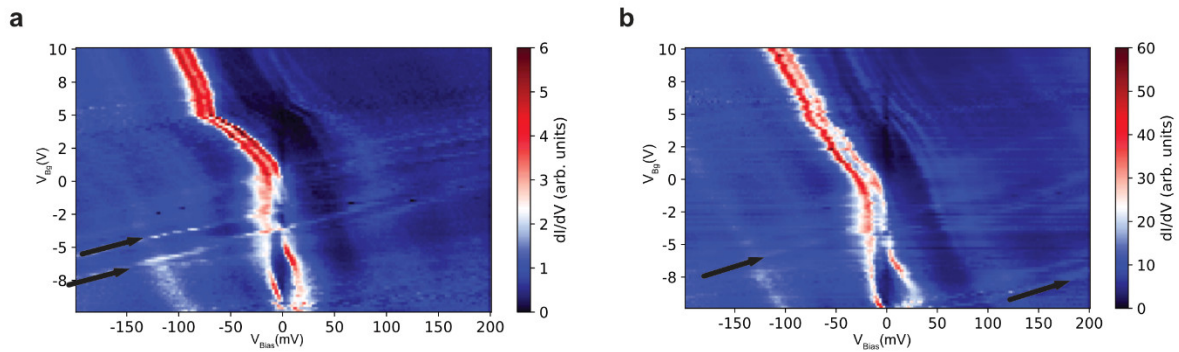


Figure S5: Spectroscopy of the AA site of device D2 for 100pA (a) and 1nA (b). Black arrows indicate resonances originating due to a tip-induced quantum dot. Note that the overall position of the point where the flat bands start crossing the Fermi level ( $V_{\text{Bias}} = 0\text{mV}$  line) as well as the charge neutrality point shift towards more negative back-gate voltages. The data are taken in the area corresponding to  $\theta = 1.03^\circ$  ( $L_{\text{MA}} = 13.9\text{nm}$ ;  $L_{\text{MB}} = 13.7\text{nm}$ ;  $L_{\text{MC}} = 13.6\text{nm}$ )

#### Section 4: Tip-gating correction at the CNP and the enhancement of the width

The slope of the lines identified to correspond to constant density can be used to correct the effects of tip gating by explicitly offsetting the back-gate voltage. Fig S6 (a,b) shows the example of this procedure applied for device D1 data. While in the uncorrected image (Fig. S6a) the constant-density lines are sloped (see the lines starting from  $V_{BG} \approx 0V$ ;  $V_{Bias} = -100mV$  in the Fig.

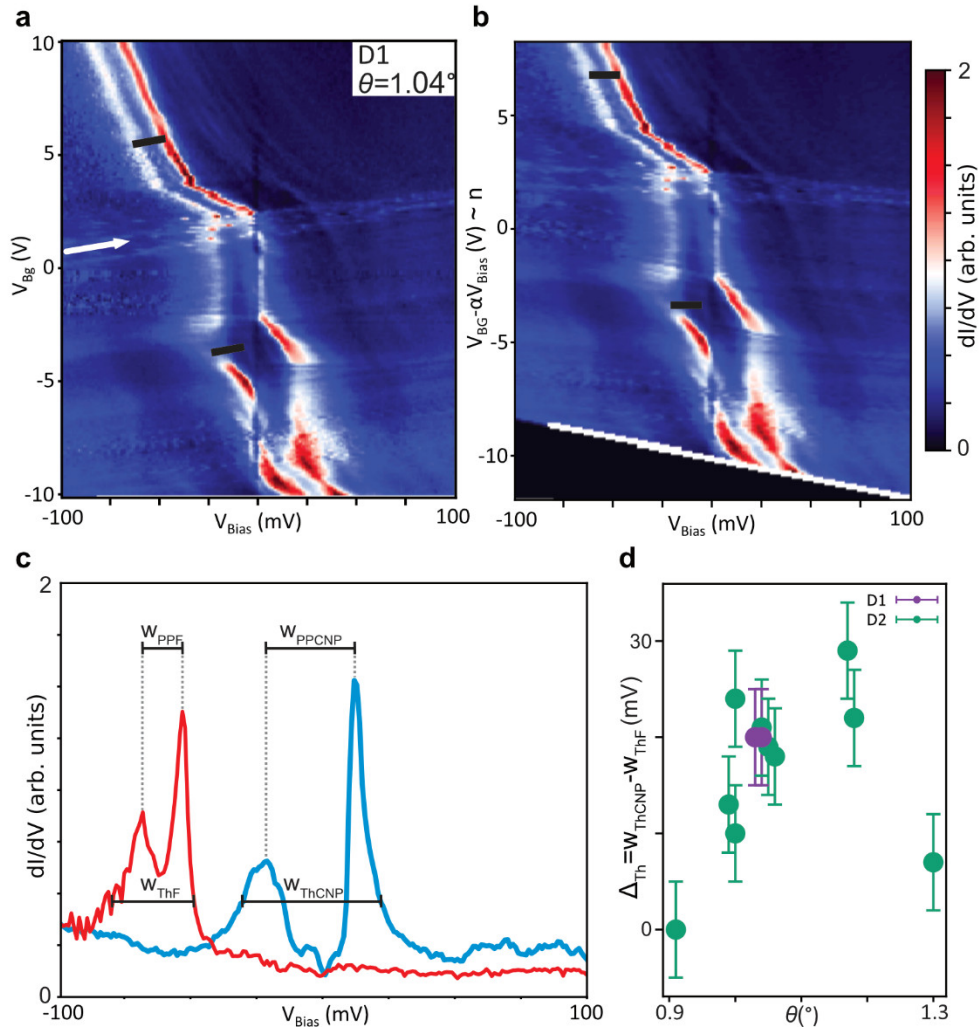


Figure S6: Device D1 data before (a) and after the linear offset correction (b). The corrected electron density is not affected by the gating of the tip. (c) Line traces from (b): Blue trace taken at the CNP; Red trace at full filling. Both the peak-to-peak distance as well as overall width of the bands increases near the CNP. (d) Energy difference between threshold widths at the CNP and full filling as a function of the angle  $\theta$ .

S6a), in the corrected data the constant density lines are horizontal indicating decoupling between the bias voltage and the carrier density. The correction cancels the influence of the tip gating on the splitting between the TDOS peaks as well as the peak bandwidth. Importantly, even after this correction *correlations effects i.e. enhanced splitting of the TDOS peaks and increased bandwidth (defined as width at certain threshold  $dI/dV$  value, see Fig. S6(c,d)) near the CNP, are still present*. We note that precise position of the TDOS peaks (data plotted in the main text Fig. 2e) are highly spatially dependent while the width at the threshold value set to be 20%-30% of the peak (at full filling) depends weakly on the spatial position around AA site. Regardless of the details such as threshold value, both the difference between threshold widths  $\Delta_{Th}=W_{ThCNP}-W_{ThFF}$  (shown in Fig. S6d) and the difference between TDOS peak positions  $\Delta_{PP}=W_{PPCNP}-W_{PPFF}$  (shown in Fig. 2e of the main text) are maximized around the magic angle value  $\theta=1.1^\circ\pm 0.1$ .

## Section 5: Areas with different twist angle $\theta$

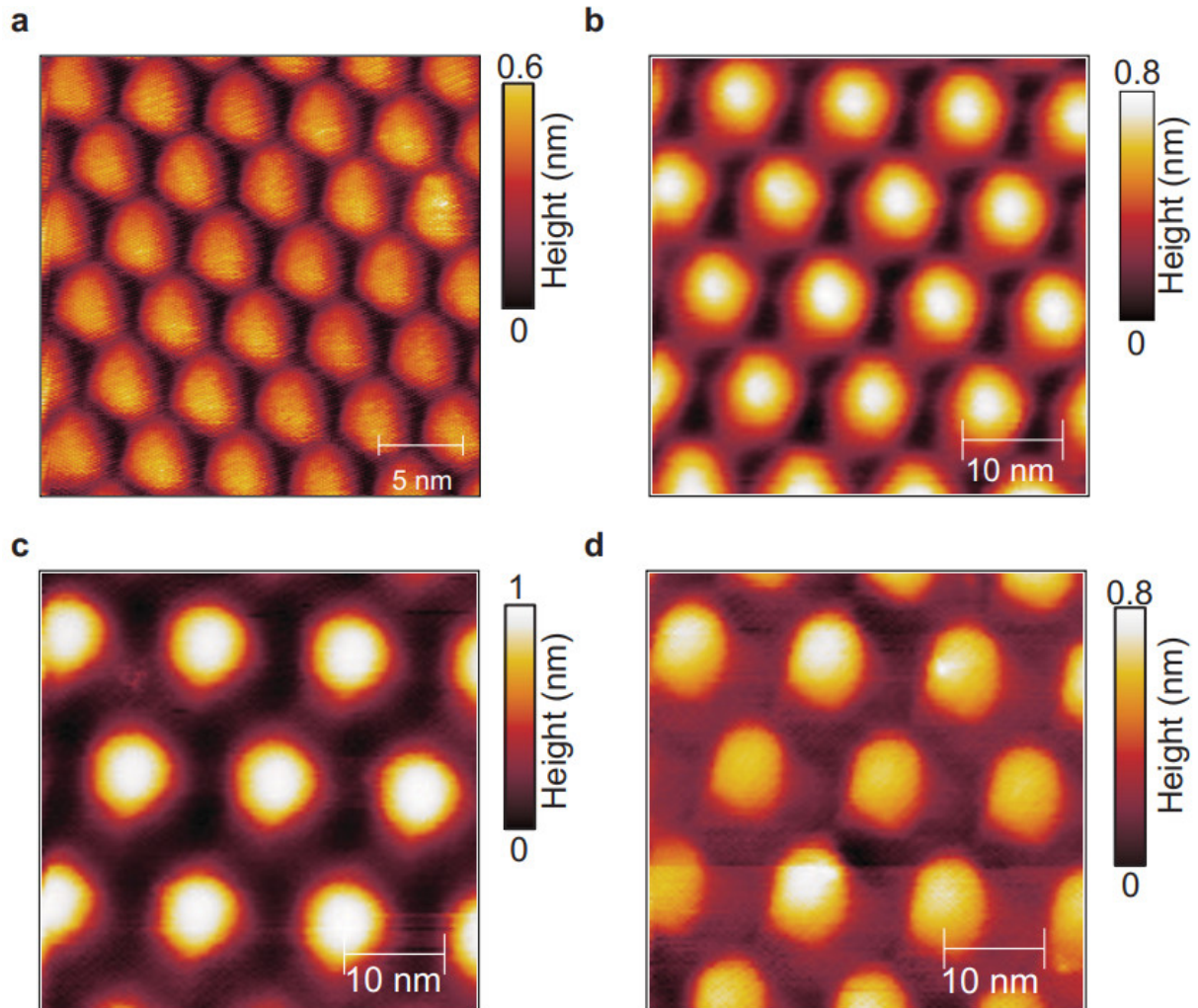


Figure S7. Examples of different areas of device D2 with twist angle  $\theta = 2.92^\circ$  (a);  $\theta = 1.31^\circ$  (b);  $\theta = 0.97^\circ$  (c);  $\theta = 1.07^\circ$  (d). Set point conditions:  $V_s = -200\text{mV}$  and  $I_s = 30\text{pA}$  (a,b);  $I_s = 100\text{pA}$  (c,d). In all samples we typically find small clean areas with the lateral size of 50nm for which the angle  $\theta$  is constant. Larger-scale areas show significant amount of fabrication residues and strain.

## Section 6: Additional data

### Line cuts from device D1

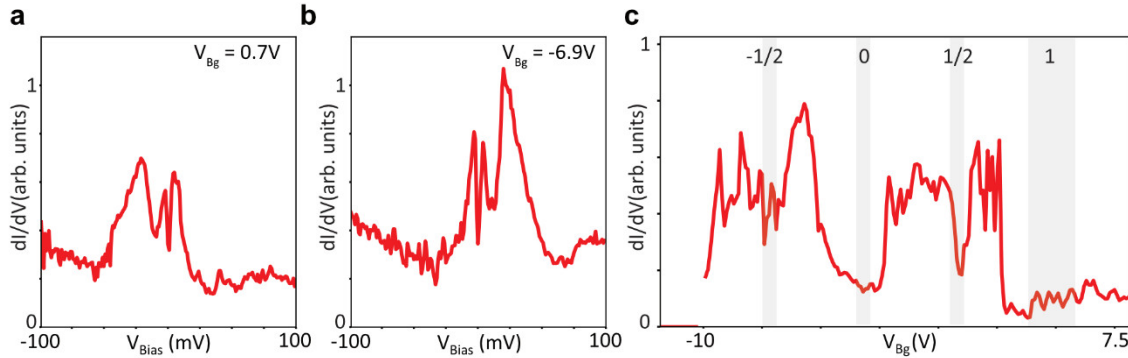


Figure S8: Linecuts from Fig. S6b corresponding to device D1,  $\theta=1.04^\circ$  in Fig. 2 of the main text. (a,b) Linecuts corresponding to  $V_{\text{Bg}} = 0.7\text{V}$  and  $V_{\text{Bg}} = -6.9\text{V}$  (corrected for tip gating) showing suppression of the local density of states close to half filling. (c) Line cut across zero bias. The gray areas indicate approximate positions of CNP, half-filling and full filling states. We note that extracting filling factors using the position of the half filling states leads to a  $15\pm 1\text{V}$  range corresponding to  $8e/A$  ( $A$  being a moiré unit cell area). This estimate is about 15% higher than the estimated value in the main text extracted from the back-gate voltage values when TDOS peaks cross Fermi level. This level of discrepancy between values obtained using different methods is in line with the transport experiments that also report variations of the positions of the half-filling states compared to the full filling. In STM measurements such discrepancy may originate from nearby defects induced by strain or relatively small area with constant twist angle.

### Additional conductance map data for device D2

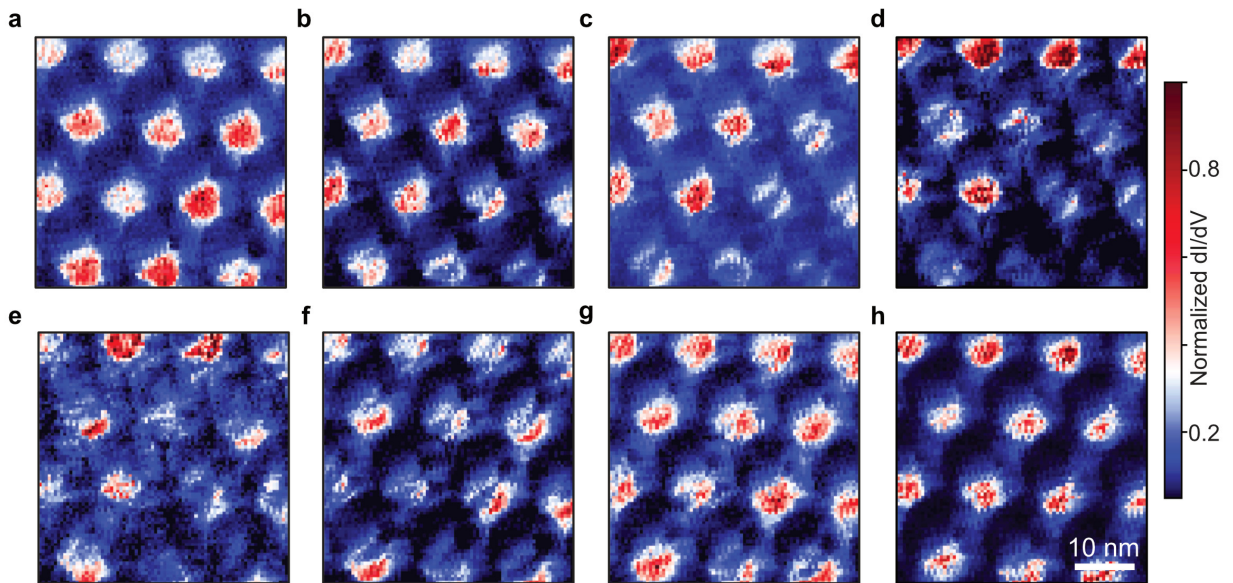


Figure S9: Conductance map close to the CNP ( $V_{\text{Bg}} = -4.5\text{V}$ ) for device D2,  $\theta=1.01^\circ$ . The data is taken with feedback off and setpoint conditions  $V_{\text{Bias}} = 500\text{ mV}$ ;  $I = 200\text{ pA}$ . The  $V_{\text{Bias}}$  voltages corresponding to panels (a-h) are: (a) -18 mV;(b) -12 mV;(c) -8 mV;(d) -4 mV; (e) 0mV (f) 8mV;(g) 12 mV;(h) 16mV.

## Section 7: Theoretical modeling

In this section we describe the theoretical model used to study the exchange effects in twisted bilayer graphene. We begin by reviewing the non-interacting Hamiltonian that serves as our starting point, before introducing Coulomb interactions and deriving a mean field Hamiltonian. We next present our results, and close with a brief discussion.

### A. Ten-band model for magic-angle bilayer graphene

Here, we briefly describe the ten-band model for magic-angle bilayer graphene, which was first introduced in Ref. <sup>10</sup>. It has been shown<sup>11,12</sup> that the flat bands of magic-angle bilayer graphene cannot be captured by any minimal tight-binding model involving only the flat bands while retaining all symmetries. However, a tight-binding description is able to fully respect the symmetries of the system without fine-tuning when including additional bands.

In particular, the (effective) symmetries of the twisted bilayer graphene system are triangular lattice translations,  $C_6$  rotations by  $2\pi/6$ , mirror symmetry  $M_{2y}$  (which takes  $y \rightarrow -y$ , but actually represents a layer-exchanging  $180^\circ$  rotation in  $3d$  about the  $x$ -axis), and time-reversal  $\mathcal{T}$ .

Further, because the momentum difference between the  $\mathbf{K}_{\text{lbz}}$  and  $\mathbf{K}'_{\text{lbz}}$  points of the (large) Brillouin zone (denoted “lbz”) of the microscopic graphene lattice is large compared to the moiré scale for small twist angles, states originating from each valley are effectively decoupled. This results in an effective  $U_v(1)$  valley symmetry, which enables us to focus on the electronic degrees of freedom in a single valley; the ten-band model of Ref.<sup>10</sup> takes advantage of this fact. However, given that both  $C_6$  and  $\mathcal{T}$  interchange the two valleys, only the combination  $C_6\mathcal{T}$  is a proper symmetry of a single-valley theory. It follows that the spatial symmetries of the ten-band model are generated entirely by  $C_2\mathcal{T}$ ,  $C_3$ , and  $M_{2y}$ .

Finally, the flat bands we wish to describe possess two Dirac cones (per spin, per valley) at the  $\mathbf{K}$  and  $\mathbf{K}'$  points of the (moiré) Brillouin zone. (We reserve  $\mathbf{K}$ ,  $\mathbf{K}'$ ,  $\Gamma$ , etc. to describe the points of the small moiré BZ.) The masslessness of the cones is ensured by  $C_2\mathcal{T}$  symmetry, while their location at  $\mathbf{K}$  and  $\mathbf{K}'$  is protected by  $C_3$ .

Before introducing interactions between electrons, we note that an overall scaling factor between the ten-band model and the actual physical system must be included. This factor can be obtained by comparing the flat bandwidth of the ten-band model and the separation of van Hove

singularities measured in the tunneling DOS in the energy regime far away from the CNP, where electron-interaction effects are presumably less important. We estimate this factor to be around 15. In all that follows, we keep the units set by the ten-band model, only scaling by  $\sim 15$  when comparing against experiment.

### 1. Non-interacting Hamiltonian

The ten-band model is defined on a triangular lattice with basis vectors  $\mathbf{a}_1 = (\sqrt{3}/2, -1/2)$  and  $\mathbf{a}_2 = (0, 1)$ . We write the Bravais lattice sites as  $\mathbf{r} = r_1\mathbf{a}_1 + r_2\mathbf{a}_2$  or simply as  $\mathbf{r} = (r_1, r_2)$ , where  $r_{1,2} \in \mathbb{Z}$ . Within each unit cell, there are ten orbitals which are distributed on three different sites, as indicated by the different colors in Fig. S10. Explicitly, there are three orbitals,  $p_z$ ,  $p_+$ , and  $p_-$ , on every triangular lattice site (red). Each of the three kagome sites (black) within a unit cell hosts an  $s$  orbital. Finally, both A and B sublattices of the honeycomb sites (blue) have  $p_+$  and  $p_-$  orbitals. Throughout this work, these ten orbitals are ordered as  $c_{\mathbf{r}} = (\tau_{z,\mathbf{r}}, \tau_{+,\mathbf{r}}, \tau_{-,\mathbf{r}}, \kappa_{1,\mathbf{r}}, \kappa_{2,\mathbf{r}}, \kappa_{2,\mathbf{r}}, \eta_{A+,\mathbf{r}}, \eta_{A-,\mathbf{r}}, \eta_{B+,\mathbf{r}}, \eta_{B-,\mathbf{r}})^T$ , where  $\tau$ ,  $\kappa$ , and  $\eta$  respectively denote operators on the triangular, kagome, and honeycomb sites.

The Bloch Hamiltonian of the ten-band model can be written as

$$\mathcal{H} = \sum_{\mathbf{k}} \sum_{i,j=1}^{10} c_{i\mathbf{k}}^\dagger H_{ij}(\mathbf{k}) c_{j\mathbf{k}}, \quad (\text{S1})$$

where  $\mathbf{k}$  is the Bloch momentum,  $i, j$  are the orbital indices, and  $c_j(\mathbf{k})$  annihilates an electron on orbital  $j$  at momentum  $\mathbf{k}$ . In our conventions the real-space and momentum-space electron operators are related via  $c_{i,\mathbf{r}} = \sum_{\mathbf{k}} \exp(i\mathbf{k} \cdot \mathbf{r}) c_i(\mathbf{k}) / \sqrt{\mathcal{V}}$ , with  $\mathcal{V}$  the area of the system.

The  $10 \times 10$  Hamiltonian matrix  $H(\mathbf{k})$  is defined as a sum of two terms

$$H(\mathbf{k}) = H_0(\mathbf{k}) + V(\mathbf{k}). \quad (\text{S2})$$

The first term,  $H_0(\mathbf{k})$ , describes hoppings from the honeycomb sites to the triangular and kagome sites; this piece takes the form

$$H_0(\mathbf{k}) = t \begin{pmatrix} 0_{6 \times 6} & h(\mathbf{k}) \\ h(\mathbf{k})^\dagger & 0_{4 \times 4} \end{pmatrix}, \quad (\text{S3})$$

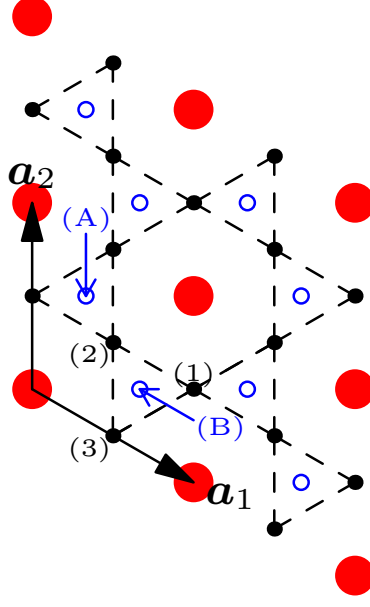


Figure S10. Lattice and orbitals for the ten-band model. The red solid circles denote the triangular sites with  $p_z$ ,  $p_+$ , and  $p_-$  orbitals. The black solid circles correspond to the three types of kagome sites, labeled as (1), (2), and (3). On each of these kagome sites, there is an  $s$  orbital. The blue empty circles indicate the honeycomb sites, either type A or type B, with  $p_+$  and  $p_-$  orbitals on each of them.

with

$$h(\mathbf{k}) = \begin{pmatrix} (1 + \phi_{11}\omega^* + \phi_{01}\omega)\zeta^*a & -(\omega + \phi_{11}\omega^* + \phi_{01})\zeta^*a & -(\omega + \phi_{10} + \phi_{11}\omega^*)\zeta a & (\omega + \phi_{10}\omega^* + \phi_{11})\zeta a \\ (1 + \phi_{11} + \phi_{01})c & (\omega^* + \phi_{11}\omega + \phi_{01})\zeta b & (1 + \phi_{10} + \phi_{11})c & (\omega^* + \phi_{10}\omega + \phi_{11})\zeta^*b \\ (1 + \omega\phi_{11} + \omega^*\phi_{01})\zeta b & (1 + \phi_{11} + \phi_{01})c & (\omega^* + \phi_{10} + \phi_{11}\omega)\zeta^*b & (1 + \phi_{10} + \phi_{11})c \\ -i\phi_{10}d & -i\phi_{10}d & id & id \\ -i\omega^*d & -i\omega d & i\omega^*d & i\omega d \\ -i\phi_{01}\omega d & -i\phi_{01}\omega^*d & i\omega d & i\omega^*d \end{pmatrix}, \quad (\text{S4})$$

where  $\phi_{\ell m} = \exp(-i(\ell k_1 + m k_2))$ ,  $k_i = \mathbf{k} \cdot \mathbf{a}_i$ ,  $\bar{\ell} = -\ell$ ,  $\omega = \exp(i2\pi/3)$  and  $\zeta = \exp(i\pi/3)$ .

The remaining tunneling amplitudes are included in the second term,  $V(\mathbf{k})$ , which can be written as

$$V(\mathbf{k}) = \begin{pmatrix} \mu_{p_z} & \mathcal{C}_{p_{\pm}p_z}^\dagger & 0 & 0 \\ \mathcal{C}_{p_{\pm}p_z} & H_{p_{\pm}} + \mu_{p_{\pm}}\mathbb{I}_{2 \times 2} & \mathcal{C}_{\kappa p_{\pm}}^\dagger & 0 \\ 0 & \mathcal{C}_{\kappa p_{\pm}} & \mu_{\kappa}\mathbb{I}_{3 \times 3} & 0 \\ 0 & 0 & 0 & H_{\eta} \end{pmatrix}. \quad (\text{S5})$$

Table I. Parameters for the ten-band model.

$t_0$	$a$	$b$	$c$	$d$	$t_\eta$	$\mu_{p_z}$	$t_{p_\pm}$	$t_{p_\pm p_\pm}$	$\mu_{p_\pm}$	$\mu_\kappa$	$t_{p_\pm p_z}$	$t_{\kappa p_\pm}^+$	$t_{\kappa p_\pm}^-$
130.0 meV	0.110	0.033	0.033	0.573	32.5 meV	$-0.1t_\eta$	$0.003t_\eta$	$0.004t_\eta$	$3t_{p_\pm}$	$0.11t_\eta$	$0.016t_\eta$	$0.016t_\eta$	$-0.016t_\eta$

Here  $\mathbb{I}$  denotes the identity matrix, and we have defined

$$H_{p_\pm} = \begin{pmatrix} t_{p_\pm} (\phi_{01} + \phi_{11} + \phi_{10} + h.c.) & t_{p_\pm p_\pm} (\phi_{01} + \omega^* \phi_{\bar{1}\bar{1}} + \omega \phi_{10}) \\ t_{p_\pm p_\pm} (\phi_{0\bar{1}} + \omega \phi_{11} + \omega^* \phi_{\bar{1}0}) & t_{p_\pm} (\phi_{01} + \phi_{11} + \phi_{10} + h.c.) \end{pmatrix} \quad (\text{S6})$$

to describe the  $p_\pm$  orbitals on the triangular sites and

$$H_\eta = t_\eta \begin{pmatrix} 0 & i(1 + \phi_{0\bar{1}} + \phi_{10}) \\ -i(1 + \phi_{01} + \phi_{\bar{1}0}) & 0 \end{pmatrix} \otimes \mathbb{I}_{2 \times 2} \quad (\text{S7})$$

to describe the honeycomb orbitals. Moreover, the coupling between the  $p_\pm$  and  $p_z$  orbitals on the triangular sites, and the coupling between  $s$  orbitals of the kagome sites and  $p_\pm$  of the triangular sites, are respectively described by

$$C_{p_\pm p_z} = it_{p_\pm p_z} \begin{pmatrix} \phi_{01} + \phi_{\bar{1}\bar{1}}\omega + \phi_{10}\omega^* \\ -(\phi_{0\bar{1}} + \phi_{11}\omega^* + \phi_{\bar{1}0}\omega) \end{pmatrix}, \quad (\text{S8})$$

and

$$C_{\kappa p_\pm} = t_{\kappa p_\pm}^+ \begin{pmatrix} \phi_{\bar{1}0} & \phi_{\bar{1}\bar{1}} \\ \phi_{\bar{1}\bar{1}}\omega^* & \omega \\ \omega & \phi_{\bar{1}0}\omega^* \end{pmatrix} - t_{\kappa p_\pm}^- \begin{pmatrix} \phi_{\bar{1}\bar{1}} & \phi_{\bar{1}0} \\ \omega^* & \phi_{\bar{1}\bar{1}}\omega \\ \phi_{\bar{1}0}\omega & \omega^* \end{pmatrix}. \quad (\text{S9})$$

Table I lists the parameters for the ten-band model.

## 2. Symmetries

As we discussed above, the model introduced in the previous section preserves the symmetries twisted bilayer graphene should possess at small angles:  $C_2\mathcal{T}$ ,  $C_3$ , and  $M_{2y}$ . In the following, we explicitly describe the action of these on the degrees of freedom in our model.

*a.*  $C_2\mathcal{T}$ : Under  $C_2\mathcal{T}$ , the basis vectors transform as

$$C_2\mathcal{T} : \quad \mathbf{a}_1 \rightarrow -\mathbf{a}_1, \quad \mathbf{a}_2 \rightarrow -\mathbf{a}_2, \quad i \rightarrow -i. \quad (\text{S10})$$









The matrix  $W$  is obtained by substituting  $c_{i\mathbf{k}} = \sum_a U_{ia}(\mathbf{k})f_{a\mathbf{k}}$ :

$$W_{ij} = -\frac{2E_C}{\mathcal{V}} \sum_{\mathbf{p}} \sum_{i,j} L_{ij} U_{aj}^\dagger(\mathbf{p}) \langle f_{a\mathbf{p}}^\dagger f_{b\mathbf{p}} \rangle U_{ib}(\mathbf{p}) = -\frac{2E_C}{\mathcal{V}} \sum_{\mathbf{p}} \sum_{i,j} L_{ij} U_{ia}(\mathbf{p}) n(\epsilon_a(\mathbf{p})) U_{aj}^\dagger(\mathbf{p}) \quad (\text{S28})$$

where  $n(\epsilon)$  is the Fermi distribution. Importantly, the modes  $f_{a\mathbf{k}}$  and the corresponding unitary matrices are implicitly functions of  $W_{ij}$ . Self-consistency requires that for a given electron filling fraction,  $n_f$ ,  $W_{ij}$  is returned when the right-hand side of Eq. (S28) is calculated using the matrices which diagonalize  $\tilde{H} = H + W$ .

Numerically, we solve this iteratively for every filling  $n_f$  under consideration. We start with  $\tilde{H}^{(0)}(\mathbf{k}) = H(\mathbf{k})$ . Diagonalizing, we obtain the energies  $\epsilon^{(0)}(\mathbf{k})$  and matrices  $U^{(0)}(\mathbf{k})$ , allowing us to determine the chemical potential  $\mu^{(0)}$  corresponding to the desired filling  $n_f$ . With this, we can then compute  $W^{(0)}$ . We subsequently define a new mean field Hamiltonian  $\tilde{H}^{(1)}(\mathbf{k}) = H(\mathbf{k}) + W^{(0)}$ . Again, we diagonalize to obtain new energies and rotation matrices,  $\epsilon^{(1)}(\mathbf{k})$  and  $U^{(1)}(\mathbf{k})$ , allowing us to determine the chemical potential,  $\mu^{(1)}$ , corresponding to  $n_f$ . Inserting this data into the right-hand-side of Eq. (S28), we find a new matrix  $W^{(1)}$ . If  $\|W^{(1)} - W^{(0)}\| = 0$  up to some threshold, we have found the mean field solution. If not, we repeat these steps until  $\|W^{(n)} - W^{(n-1)}\| = 0$  is satisfied.

In general more than one self-consistent solution  $W$  exists. Further, some of these solutions result in ground states which spontaneously break some of the symmetries of the Hamiltonian. To take these into account, we alter the non-interaction Hamiltonian in the first step,  $\tilde{H}^{(0)}(\mathbf{k}) = H(\mathbf{k}) + \delta H(\mathbf{k})$ , where  $\delta H(\mathbf{k})$  transforms non-trivially under one or more of the symmetries. While  $\delta H(\mathbf{k})$  is not included in any subsequent step, initializing in this fashion allows the simulation to find symmetry-broken solutions should they exist.

More explicitly, this perturbation takes the form

$$\delta H(\mathbf{k}) = \sum_G \alpha_G \mathcal{O}_G(\mathbf{k}) \quad (\text{S29})$$

where  $G$  is a symmetry group element,  $\alpha_G$  are small numbers relative to the flat bandwidth, and  $\mathcal{O}_G(\mathbf{k})$  are the momentum components of an operator, or ‘‘order parameter,’’ which transforms nontrivially under the symmetry  $G$  and trivially under all others. Ideally, we would like to restrict to the generators of the symmetry group:  $G = C_2\mathcal{T}, C_3, M_{2y}$ . However, it turns out that the best way to seed  $C_2\mathcal{T}$  symmetry-breaking is through a joint  $C_2\mathcal{T}, M_{2y}$  order parameter. Because

the flat band wavefunctions are primarily located on the triangular lattice sites, we consider order parameters located on these sites as well. In particular, the ones we use are:

$$\begin{aligned}
\mathcal{O}_{C_2\mathcal{T}\cdot M_{2y}} &= \sum_{\mathbf{r}} \left( \tau_{+,r}^\dagger \tau_{+,r} - \tau_{-,r}^\dagger \tau_{-,r} \right) = \sum_{\mathbf{k}} \left( \tau_{+,k}^\dagger \tau_{+,k} - \tau_{-,k}^\dagger \tau_{-,k} \right), \\
\mathcal{O}_{C_3} &= \sum_{\mathbf{r}} \left( \tau_{+,r+a_2}^\dagger + \tau_{+,r-a_1-a_2}^\dagger + \tau_{+,r+a_1}^\dagger \right) \tau_{-,r} + h.c. \\
&= \sum_{\mathbf{k}} (\phi_{01} + \phi_{10} + \phi_{11}^*) \tau_{+,k}^\dagger \tau_{-,k} + h.c. \\
\mathcal{O}_{M_{2y}} &= \sum_{\mathbf{r}} i \left( \tau_{+,r+a_1}^\dagger + \omega \tau_{+,r+a_2}^\dagger + \omega^* \tau_{+,r-a_1-a_2}^\dagger \right) \tau_{-,r} + h.c. \\
&= \sum_{\mathbf{k}} i (\phi_{01} + \omega \phi_{10} + \omega^* \phi_{11}) \tau_{+,k}^\dagger \tau_{-,k} + h.c.
\end{aligned} \tag{S30}$$

where  $\phi_{\ell m} = e^{-i(\ell k_1 + m k_2)}$ .

### C. Results

At certain  $n_f$ , we find a number of different solutions to the mean field equation, and these can be classified by their symmetry-breaking behaviour. There are three general classes: those which preserve all the symmetries, those which break  $C_3$  but preserve  $C_2\mathcal{T}$  and  $M_{2y}$  and those which break  $C_2\mathcal{T}$  and  $M_{2y}$  (we find that these two symmetries are always broken together). There are further distinctions within each class. For instance, for those solutions with  $C_3$  symmetry breaking, two distinct symmetry breaking patterns are found – one of these is shown in Fig. 3 of the main text. Similarly, for the solutions which break  $C_2\mathcal{T}$  and  $M_{2y}$ , there are two solutions which also break  $C_3$  and one which does not.

The ground state at a filling  $n_f$  is given by the solution with the lowest energy. In Fig. S11(a), we show the ground state energy  $E_0$  per unit cell per flavour as a function of filling  $n_f$  for these six solutions. For  $n_f \lesssim -0.5$  and  $n_f \gtrsim 0.5$ , we see that the energies converge to a single value. Close to charge neutrality, the energies of the symmetry-broken states dip below that of the symmetric state in a non-trivial fashion. The difference between the ground state energy of the symmetry-broken solutions and the symmetric solution is displayed in Fig. S11(b).

We now discuss each of these solutions in turn.

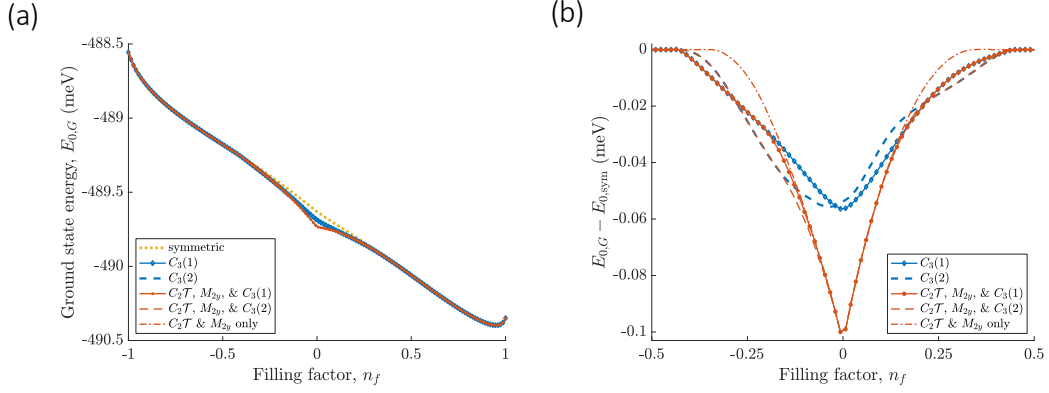


Figure S11. (a) Ground state energy per unit cell per flavour as a function of filling  $n_f$  for the three general classes of solutions. The yellow dotted line plots the energy of the symmetric solution. The two blue lines display the energies of the two solution with  $C_3$ -breaking only, while the three red lines plot the energies of the  $C_2\mathcal{T}$ -broken solutions (including those which also break  $C_3$ ). (b) The difference in ground state energies between the symmetry-broken solutions and the symmetric solution.

### 1. Fully symmetric

When we initialize with  $\delta H = 0$ , no symmetry-breaking can occur. We will refer to this solution as  $\mathcal{S}.sym$ . The resulting density of states as a function of filling and energy is shown in Fig. S12(a) while linecuts of the density of states at  $n_f = 0$  and  $n_f = 1$  are shown in (b). Both (a) and (b) indicate that the density of states changes very little as a function of filling.

### 2. $C_3$ breaking only

By initializing our Hamiltonian with  $\delta H = \alpha_{C_3} \mathcal{O}_{C_3}$  ( $\mathcal{O}_{C_3}$  is given in Eq. (S30)), depending on the sign of  $\alpha_{C_3}$  we choose, two distinct  $C_3$ -breaking solutions are obtained close to charge neutrality. When  $\alpha_{C_3} < 0$ , we obtain the density of states shown in Fig. S13(a). Unlike the symmetric case, there is significant splitting between the peaks close to charge neutrality. This is further emphasized by Fig. S13(b), where linecuts of the DOS at  $n_f = 0$  and  $n_f = 1$  are shown. We refer to this set of solutions as  $\mathcal{S}.C_3(1)$ . (We note that these figures have already been shown in Figs. 3(A)-(C) of the main text.)

Conversely, when  $\alpha_{C_3} > 0$ , a separate set of solutions, termed  $\mathcal{S}.C_3(2)$ , is obtained. The re-

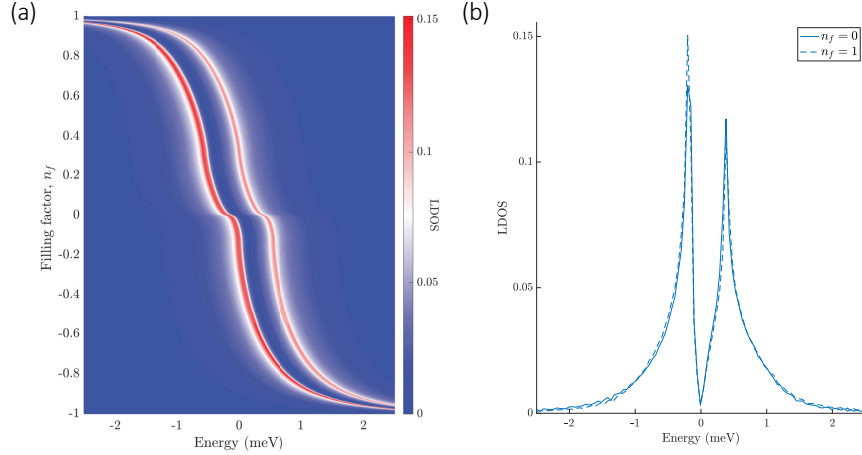


Figure S12. (a) Local density of states of the symmetry-preserving solution. (b) A linecut of the density at the charge neutrality point,  $n_f = 0$ , (solid line) and with a fully-filled flat band,  $n_f = 1$  (dashed line). The linecut at  $n_f = 1$  has been shifted so the Dirac points occur at zero energy.

sulting DOS is shown in Fig. S13(e) and a linecut at  $n_f = 0$  and 1 is provided in (f). As with  $\mathcal{S}.C_3(1)$ , both peak broadening and peak separation are observed in the region surrounding charge neutrality. Compared to Fig. S13(e), the splitting of the lower-band peak (left side of plot) is substantially less pronounced than it is for the  $\mathcal{S}.C_3(1)$  solution in (a). This is also clear from the density linecuts in Figs. S13(b) and (f).

We verify that the differences between Figs. S13(a) and (e) on the one hand and the DOS of the symmetric solution in Fig. S12(a) on the other can be accounted for by  $C_3$  breaking by plotting the absolute values of the expectation values of the three order parameters in Eq. (S30). The results are shown in Figs. S13(c) and (g) for  $\mathcal{S}.C_3(1)$  and (2) respectively. In both,  $|\langle \mathcal{O}_{C_2\mathcal{T}.M_{2y}} \rangle|$  vanishes for all  $n_f$ , while  $|\langle \mathcal{O}_{C_3} \rangle|$  is nonzero for  $-0.5 \lesssim n_f \lesssim 0.5$ . The conservation of  $C_2\mathcal{T}$  and  $M_{2y}$  and the breaking of  $C_3$  has also been explicitly demonstrated by studying the symmetry transformation properties of the corresponding mean field Hamiltonians. We conclude that within the interval  $-0.5 \lesssim n_f \lesssim 0.5$ , only  $C_3$  is broken and that outside of it, all symmetries are preserved.

These results are in conjunction with the observation that the density of states in Figs. S13(a) and (e) and Fig. S12(a) are identical when  $n_f \lesssim -0.5$  or  $n_f \gtrsim 0.5$ . Analogously, in Fig. S11 the ground state energies of  $\mathcal{S}.C_3(1)$  and (2) converge to the same value as the symmetric solution for these fillings.

At charge neutrality, both  $\mathcal{S}.C_3(1)$  and  $\mathcal{S}.C_3(2)$  are lower in energy than the symmetric solution

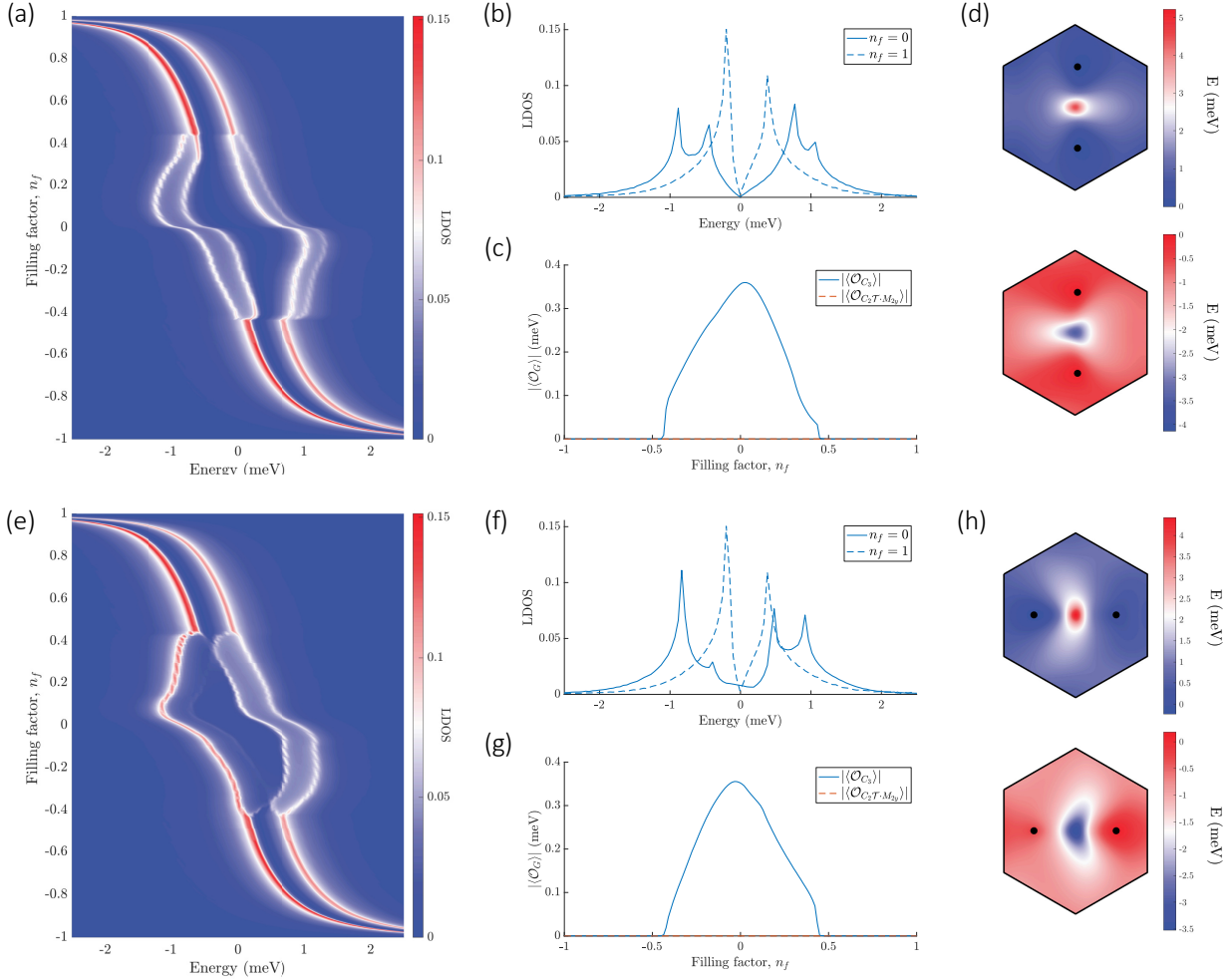


Figure S13. Plot of  $C_3$ -breaking solutions which preserve  $M_{2y}$  and  $C_2\mathcal{T}$ . (a)-(d) correspond to  $\mathcal{S}.C_3(1)$ , while (e)-(h) correspond to  $\mathcal{S}.C_3(2)$ . (a),(b) Density of states as a function of filling and energy. (b),(f) Linecut at  $n_f = 0$  (solid) and  $n_f = 1$  (dashed). The linecut at  $n_f = 1$  has been shifted so the Dirac points occur at zero energy. (c),(g) Magnitude of the  $C_3$  and  $C_2\mathcal{T} \cdot M_{2y}$  order parameter expectation values. (d),(h) Mean field band structure within the moiré BZ obtained at charge neutrality. The top plot corresponds to the flat band and the bottom plot to the lower flat band. The Dirac points are indicated by the black dots.

by  $\sim 0.05$  meV. While Fig. S11 shows that when  $n_f > 0$ ,  $\mathcal{S}.C_3(1)$  is preferred over  $\mathcal{S}.C_3(2)$  and vice versa for  $n_f < 0$ , the two solutions are always very close in energy, with a maximal energy difference of  $\sim 0.01$  meV. Given that strain is expected to be of order 0.03 meV (taking into account the scaling factor of 15), we should not attempt to distinguish the two based on energetics.

Since neither symmetry nor ground state energy can differentiate  $\mathcal{S}.C_3(1)$  and (2), we plot the

band structures obtained at charge neutrality in Figs. S13(d) and (h). As mentioned above, the  $C_2\mathcal{T}$  symmetry protects the Dirac cones, while  $C_3$  protects their location. Accordingly, as indicated by the black dots, the Dirac cones remain but are no longer located at the  $\mathbf{K}$  and  $\mathbf{K}'$  points. Here, a clear difference between  $\mathcal{S}.C_3(1)$  and (2) is observed: The Dirac cones of  $\mathcal{S}.C_3(1)$  lie close to the  $y$ -axis and are interchanged under  $M_{2y}$ , but those of  $\mathcal{S}.C_3(2)$  are on the  $x$ -axis, and so are mapped to themselves under  $M_{2y}$ .

While both solutions are clearly  $M_{2y}$  symmetric, the solution  $\mathcal{S}.C_3(2)$  cannot be continuously connected to the non-interacting band structure without breaking the  $M_{2y}$  symmetry. This was our primary motivation for choosing to show the density of states given by  $\mathcal{S}.C_3(1)$  in the main text.

*a. Spatial map of local density of states* One way to probe  $C_3$  breaking experimentally is to map out the spatial profile of the local density of states in real space at a given bias voltage by the STM tip. Theoretically, this local density of states  $\rho(\mathbf{r}; E)$  at location  $\mathbf{r}$  and bias voltage  $V_{\text{bias}} = E$  is encoded in the imaginary part of the real-space local Green's function,  $G(E; \mathbf{r}, \mathbf{r})$

$$\rho(\mathbf{r}) = -\frac{1}{\pi} \lim_{\eta \rightarrow 0^+} \text{Im} G(E + i\eta; \mathbf{r}, \mathbf{r}). \quad (\text{S31})$$

For a tight-binding model, such as the ten-band model used in this work, only the local density of states of a particular orbital on a given sublattice is well-defined. For a system with translational invariance with periodic boundary condition, the real-space local Green function for the ten-band model with mean-field-decoupled interaction is given by

$$G(E) = \frac{1}{\mathcal{V}} \sum_{\mathbf{k}} \left[ E - \tilde{H}(\mathbf{k}) \right]^{-1}, \quad (\text{S32})$$

which is a  $10 \times 10$  matrix in the basis of the 10 orbitals within a unit cell. Note that  $G(E)$  is defined within a single unit cell and it will be the same in every unit cell across the whole system, due to translational invariance.

The local density of states  $\rho_\alpha$  of a particular orbital  $\alpha$  within a unit cell is defined as

$$\rho_\alpha(E) = -\frac{1}{\pi} \lim_{\eta \rightarrow 0^+} \text{Im} G_{\alpha\alpha}(E). \quad (\text{S33})$$

Although the spectral weight of the flat bands is mainly located on the triangular sites, the  $\rho_\alpha(E)$  with  $\alpha$  corresponding to the three kagome sites does contain information on whether  $C_3$  symmetry is present in the system. This is due to the fact that under  $C_3$ , the three orbitals on the kagome

sites transform as  $\kappa_1 \rightarrow \kappa_2$ ,  $\kappa_2 \rightarrow \kappa_3$ , and  $\kappa_3 \rightarrow \kappa_1$ , and so do the  $\rho_\alpha(E)$  on these orbitals. Thus, the local density of states will be the same on the three types of kagome sites in our ten-band model when  $C_3$  symmetry is present. However, when  $C_3$  is broken but  $M_{2y}$  is preserved, as in the case of Fig. 3 of the main text,  $\rho_{\kappa_1}(E)$  can differ from  $\rho_{\kappa_2}(E)$  and  $\rho_{\kappa_3}(E)$ , while the latter two are the same because of  $M_{2y}$  symmetry. It is worth mentioning that, at least to some extent, the local density of states at the three kagome sites simulates the local density of states measured experimentally in between two moiré (triangular) sites, which are oriented along three directions. In Fig. 3F of the main text, we have plotted the  $\rho_\alpha$  as widths of the bonds between triangular sites, which can be compared with the experimental map of the local density of states.

### 3. $C_2\mathcal{T}/M_{2y}$ breaking

We find three distinct solutions which break both the  $C_2\mathcal{T}$  and  $M_{2y}$  symmetries. Note that  $C_2\mathcal{T}$ -broken phases at neutrality were also found very recently in a continuum model with realistic Coulomb interaction<sup>16</sup>. While the sign of  $\alpha_{C_2\mathcal{T}\cdot M_{2y}}$  does not affect the state, different results are obtained depending on whether  $C_3$  is allowed to break and, if so, the sign of  $\alpha_{C_3}$ . The density of states obtained by initializing with  $\alpha_{C_3} < 0$ ,  $\alpha_{C_3} > 0$ , and  $\alpha_{C_3} = 0$  are respectively shown in Figs. S14(a), (b), and (c). We refer to these solutions as  $\mathcal{S}\cdot C_2\mathcal{T}\cdot C_3(1)$ ,  $\mathcal{S}\cdot C_2\mathcal{T}\cdot C_3(2)$ , and  $\mathcal{S}\cdot C_2\mathcal{T}$ . (Since  $M_{2y}$  is broken whenever  $C_2\mathcal{T}$  is, for notational simplicity we do not include it in our naming convention.)

As observed in the previous section, away from charge neutrality,  $n_f \gtrsim 0.5$  or  $n_f \lesssim -0.5$ , all three solutions converge to the symmetric solution  $\mathcal{S}\cdot\text{sym}$ . Figures. S14(d) and (e) both demonstrate that for these fillings, the  $C_3$  and  $C_2\mathcal{T} \cdot M_{2y}$  order parameters vanish. Explicit study of the mean field Hamiltonians supports the conclusion that all solutions fully preserve the symmetries at these fillings.

We focus first on  $\mathcal{S}\cdot C_2\mathcal{T}\cdot C_3(1)$  and (2). Moving closer to charge neutrality, both Figs. S14(a) and (b) enter regions reminiscent of those found in Figs. S13(a) and (b). For  $-0.5 \lesssim n_f \lesssim -0.2$  and  $0.2 \lesssim n_f \lesssim 0.5$ , only  $C_3$  is broken, as indicated in Figs. S14(d) and (e). In this region, it turns out that  $\mathcal{S}\cdot C_2\mathcal{T}\cdot C_3(1)$  and (2) are in fact identical to  $\mathcal{S}\cdot C_2\mathcal{T}\cdot C_3(1)$  and (2) respectively. Around  $n_f \sim \pm 0.25$ , however,  $|\langle \mathcal{O}_{C_2\mathcal{T}\cdot M_{2y}} \rangle|$  becomes nonzero [Fig. S14(d)]. With  $C_2\mathcal{T}$  broken, the Dirac points cease to be protected, and Fig. S14(f) shows a gap opening at this point. Continuing to-

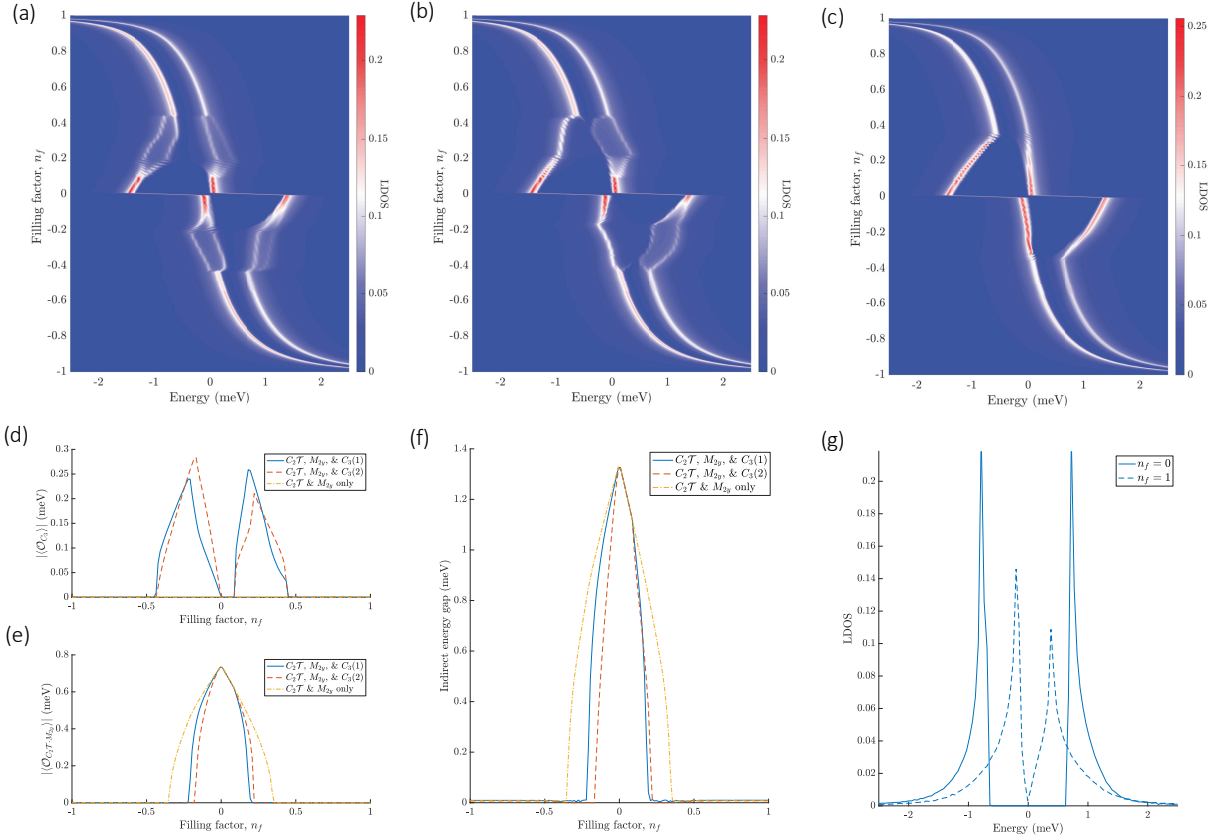


Figure S14. (a),(b),(c) Density of states for solutions  $\mathcal{S}.C_2\mathcal{T}.C_3(1)$ ,  $\mathcal{S}.C_2\mathcal{T}.C_3(2)$ , and  $\mathcal{S}.C_2\mathcal{T}$  respectively. (d) Magnitude of  $C_3$  order parameter expectation values as a function of filling. (e) Magnitude of  $C_2\mathcal{T} \cdot M_{2y}$  order parameter expectation values as a function of filling. (f) Gap as a function of filling. (g) Linecut at  $n_f = 0$  and  $n_f = 1$ . For these fillings, the three solutions in (a)-(c) are identical. The linecut at  $n_f = 1$  has been shifted so the Dirac points occur at zero energy.

towards charge neutrality, Figs. S14(d) and (e) plots the  $C_3$  and  $C_2\mathcal{T}$  order parameter expectation values decreasing and increasing, respectively, and we conclude that the  $C_3$  and  $C_2\mathcal{T}$  orders are competing. Eventually, very close to charge neutrality,  $C_3$  symmetry is completely restored in both  $\mathcal{S}.C_2\mathcal{T}.C_3(1)$  and (2).

Turning to the remaining solution,  $\mathcal{S}.C_2\mathcal{T}$ , the plot of the magnitude of the  $C_3$  order parameter in Fig. S14(d) confirms that the  $C_3$  symmetry is not broken for any filling fraction studied. Without having to compete with the  $C_3$  order, the  $C_2\mathcal{T}$  symmetry is able to break further from charge neutrality, close to  $n_f \sim \pm 0.5$  as indicated in Fig. S14(e). Again, this coincides with the opening

of the gap in (f).

Finally, at charge neutrality, all three solutions are identical and a gap is found. This is shown in Fig. S14(g).

#### D. Discussion

Based on the ten-band model with local Coulomb interaction, and within a Hartree-Fock mean-field approximation, we have found various symmetry-broken solutions. Although the  $C_2\mathcal{T}$ -broken gapped solutions are lower in ground state energy per unit cell by about 0.05 meV, the gapless  $C_3$ -broken solutions seem to be most consistent with experiment since no gap at charge neutrality is observed. The emergence of the gapless solution in experiment is plausible even when taking into account the scaling factor  $\sim 15$  between our model and the physical system. With this factor, the energy difference translates into  $\sim 7$  K, which should be smaller than the error incurred by approximating the physical system with a simple ten-band model and a specific local interaction. Finally, in a real system the  $C_3$  symmetry is presumably broken explicitly because of strain in the sample, which may make the  $C_3$ -broken solution more likely. On the other hand, breaking  $C_2\mathcal{T}$  explicitly may be much harder than  $C_3$ . Suppose that the system exhibits long-range,  $\mathcal{T}$ -preserving disorder. In this case  $C_2\mathcal{T}$  can only be explicitly broken if the disorder violates  $C_2$ . Crucially,  $C_2$  map the valleys  $\mathbf{K}_{\text{lbz}}$  and  $\mathbf{K}'_{\text{lbz}}$  of the microscopic honeycomb system to one another, and, as emphasized above, these are separated by a very large momentum compared to the flat-band scales. Hence lifting  $C_2$  symmetry requires atomic-scale deformations, whereas disorder on the moiré lattice scale would be sufficient to break  $C_3$  symmetry.

## References:

1. Kim, K. *et al.* van der Waals Heterostructures with High Accuracy Rotational Alignment. *Nano Lett.* **16**, 1989–1995 (2016).
2. Kim, K. *et al.* Tunable moiré bands and strong correlations in small-twist-angle bilayer graphene. *Proc. Natl. Acad. Sci.* **114**, 3364–3369 (2017).
3. Cao, Y. *et al.* Superlattice-Induced Insulating States and Valley-Protected Orbits in Twisted Bilayer Graphene. *Phys. Rev. Lett.* **117**, 116804 (2016).
4. Cao, Y. *et al.* Correlated insulator behaviour at half-filling in magic-angle graphene superlattices. *Nature* **556**, 80–84 (2018).
5. Wong, D. *et al.* Local spectroscopy of moiré-induced electronic structure in gate-tunable twisted bilayer graphene. *Phys. Rev. B* **92**, 155409 (2015).
6. Yankowitz, M., Watanabe, K., Taniguchi, T., San-Jose, P. & LeRoy, B. J. Pressure-induced commensurate stacking of graphene on boron nitride. *Nat. Commun.* **7**, 13168 (2016).
7. Mashoff, T. *et al.* Bistability and Oscillatory Motion of Natural Nanomembranes Appearing within Monolayer Graphene on Silicon Dioxide. *Nano Lett.* **10**, 461–465 (2010).
8. Maltezopoulos, T. *et al.* Wave-Function Mapping of InAs Quantum Dots by Scanning Tunneling Spectroscopy. *Phys. Rev. Lett.* **91**, 196804 (2003).
9. Jung, S. *et al.* Evolution of microscopic localization in graphene in a magnetic field from scattering resonances to quantum dots. *Nat. Phys.* **7**, 245–251 (2011).
10. Po, H. C., Zou, L., Senthil, T. & Vishwanath, A. Faithful Tight-binding Models and Fragile Topology of Magic-angle Bilayer Graphene. *ArXiv180802482 Cond-Mat* (2018).
11. Po, H. C., Zou, L., Vishwanath, A. & Senthil, T. Origin of Mott Insulating Behavior and Superconductivity in Twisted Bilayer Graphene. *Phys. Rev. X* **8**, 031089 (2018).

12. Zou, L., Po, H. C., Vishwanath, A. & Senthil, T. Band structure of twisted bilayer graphene: Emergent symmetries, commensurate approximants, and Wannier obstructions. *Phys. Rev. B* **98**, 085435 (2018).
13. Trambly de Laissardière, G., Mayou, D. & Magaud, L. Localization of Dirac Electrons in Rotated Graphene Bilayers. *Nano Lett.* **10**, 804–808 (2010).
14. Fang, S. & Kaxiras, E. Electronic structure theory of weakly interacting bilayers. *Phys. Rev. B* **93**, 235153 (2016).
16. Xie, M. & MacDonald, A. H. On the nature of the correlated insulator states in twisted bilayer graphene. *ArXiv181204213 Cond-Mat* (2018).